Distribution of Colloid Particles onto Interfaces in Partially Saturated Sand

YUNIATI ZEVI,† ANNETTE DATHE,† JOHN F. MCCARTHY,‡ BRIAN K. RICHARDS,† AND TAMMO S. STEENHUIS*,†

Department of Biological and Environmental Engineering, Cornell University, Ithaca, New York 14853, and Department of Earth and Planetary Sciences, University of Tennessee, Knoxville, Tennessee 37996-1410

Colloids have long been known to facilitate the transport of contaminants in soils, but few direct observations have been made of transport and retention in unsaturated porous media. Studies have typically been limited to evaluation of column breakthrough curves, resulting in differing and sometimes conflicting proposed retention mechanisms. We carried out pore scale visualization studies of colloid transport in unsaturated quartz sand to directly observe and characterize colloid retention phenomena. Synthetic hydrophilic (0.8, 2.6, and 4.8 μm carboxylated polystyrene latex) and relatively hydrophobic (5.2 μm polystyrene latex) colloidal microspheres were added to steady-state water flow (0.15 mm min^{-1}) applied to an inclined infiltration chamber. Bright field microscopy was used to determine the positions and movement of water and colloids. Confocal laser scanning microscopy was used to determine water film geometry in an unsaturated horizontal chamber. We determined mechanisms of hydrophilic colloid retention at what is generally termed the air/water/solid (AWS) interface. Based on our observations, the AWS interface is here more accurately termed the air/water meniscus/solid (AW_mS) interface, denoting the region where between-grain water meniscii diminish to thin water films on the grain surfaces. Colloids were retained at the AW_mS interface where the film thickness approximately equaled colloid diameters. The greater retention for hydrophilic colloids at this interface (compared to elsewhere in the solid/water interface) can be explained by the additional surface tension capillary potentials exerted on colloids at the AW_mS interface. While some 0.8-μm colloids were observed in thin water films, film straining played no significant role in the retention of larger colloids. Mechanisms for slightly hydrophobic colloids differed slightly. In addition to primary retention at the AW_mS interface, hydrophobic colloids attached to others already present at that interface resulting in apparent retention at the air/water (AW) interface. Attachment of hydrophobic colloids was also observed at water-solid interfaces, as hydrophobicity impelled the colloids to avoid water. Factors contributing to retention of slightly hydrophobic colloids were sand grain roughness and possibly a tendency for these colloids to flow near surfaces and interfaces, consonant with the enhanced retention of hydrophobic colloids (relative to hydrophilic colloids) observed in the literature.

* Corresponding author tel: 607-255-2489; fax: 607-255-4080; e-mail: tss1@cornell.edu.
† Cornell University.
‡ University of Tennessee.

Introduction

The transport of colloids in groundwater has been an area of active research in recent decades (*1*−*10*). Field-based results suggested the importance of colloids in the transport of low-solubility contaminants (*11*−*13*). Laboratory studies of colloid and colloid-facilitated transport have focused primarily on the interpretation of breakthrough of colloids (using latex microspheres, clays, oxides, or microorganisms, with or without other tracers) in sand or glass bead experimental systems. While most studies have been carried out under saturated flow conditions (*9*, *14*−*17*), others have examined unsaturated flow (*18*−*30*).

Direct observations of colloid transport in unsaturated porous media are limited. Wan and Wilson (*18*) employed etched glass micromodels and found that hydrophilic (both anionic and cationic) and hydrophobic colloids deposited at the air−water (AW) interface. Later theoretical work and tests with latex microspheres in bubble columns suggested that only the cationic amidine polystyrene particles would partition to the AW interface, while negatively charged sulfate and carboxylated latex colloids were excluded (*31*). Weisbrod et al. (*9*) were able to visually render colloid distributions at the Darcy scale over time, using a light transmission technique. Sirivithayapakorn and Keller (*32*) found that carboxylated polystyrene latex spheres and bacteriophage MS2 were attracted to the AW interface of trapped air bubble in micromodel pore space. Crist et al. (*33*−*35*) used a CCD camera to obtain a time sequence of colloid retention in unsaturated silica sand. Weakly anionic hydrophilic colloids were deposited at the air−water−solid (AWS) interface, and hydrophobic colloids were deposited at the water−solid (WS) interface, but neither type was found at the AW interface.

Mathematical and conceptual models were initially developed for saturated porous media (*8*, *36*−*41*) and later adapted to unsaturated media (*20*, *42*−*45*). These models usually assume that the convective dispersive equation is valid and may or may not account for preferential (or bypass) flow. Colloid deposition is included with a sink/source term. The magnitude of the sink term for colloid retention can be described as the product of two factors: (1) the collector (or contact) efficiency (η), which is the probability of a mobile particle contacting a collector surface, comprising the effects of interception, sedimentation, and Brownian motion; and (2) the collision efficiency (α), which is the probability that such a collision will result in attachment (*46*, *47*). Descriptions of colloid retention in partially saturated media are complicated by the existence of two interfaces—AW and SW (solid−water)—that can each serve as collector surfaces, albeit with distinct electrostatic and surface tension properties. In addition, water film thickness can vary under partial saturation, depending not only on the water content, but, as shown later, by the position of the film relative to the pendular rings of water between grains.

Because visualization of colloid transport is still in its infancy, colloid breakthrough curves have been used to derive various forms of sink terms. However, breakthrough curves represent an integrated response which can neither differentiate nor evaluate the relative contributions of individual colloid retention processes. Several retention mechanisms

10.1021/es048595b CCC: $30.25
Published on Web 00/00/0000

TABLE 1. Colloidal Microsphere Characteristics, Zeta Potentials (ζ), and Water Contact Angles

microsphere type	manufacturer lot and color/size code	diameter (μm)	color	H in DDI water (mV at 20 °C)	contact angle with water (deg)
carboxylated polystyrene latex(hydrophilic)	CMB2458 DDY100	0.8	blue	−31.1	<10
	CAR1225A DY200	2.6	red	−36.0	<10
	CAB2457 DY400	4.8	blue	−29.6	<10
polystyrene latex (slightly hydrophobic)	PSB 2507 DY400	5.2	blue	−44.7	20−25

leading to different forms of sink terms have been proposed. One mechanism often posited as the reason for greater colloid retention in unsaturated porous media is deposition at the AW interface based primarily on two-dimensional micromodel studies (*18*, *32*). Subsequent colloid breakthrough experiments thus attributed the observed increases in colloid retention under decreasing moisture contents to attachment at the AW interface (*19*, *20*, *22*, *28*, *29*, *43*, *48*). However, recent three-dimensional visualization studies in our group with Crist et al. (*33*−*35*) suggest that hydrophilic colloids collect at the air−water−solid (AWS) interface rather than the AW interface. Bacteriophage collection at the AWS interface had also been suggested in batch system studies (*24*).

Another colloid retention mechanism proposed is film straining (*20*), which occurs only when pendular rings become disconnected below a critical water saturation level. In this scenario, the thickness of water films that surround media grains decreases until it approaches or falls below the diameter of the colloid, thus immobilizing it in the thin water film (*20*, *49*). Equilibrium film thicknesses can be calculated from the matric potential using the Hamaker equation (*50*):

$$w = \sqrt[3]{\frac{A_{svl}}{6\pi\rho g\Psi}} \quad (1)$$

where A_{svl} is the Hamaker constant for solid−vapor−liquid interaction (-19×10^{-20} *J*), ρ is the density of water, g is the gravity acceleration, and Ψ is the matric potential. However, even under relatively moist conditions (Ψ values of −5 to −10 cm), the calculated thickness of water films is approximately 0.02 μm, which is 10- to 50-fold smaller than the diameters of colloids used in most experiments. Such films are unlikely to be able to transport and subsequently deposit colloids on grain surfaces. Furthermore, Crist et al. (*33*) observed that colloids followed retreating menisci as water saturation declined, rather than being trapped in the nanometer-thick water films remaining at the grain surfaces.

Despite increasing research in this area, it is not yet clear exactly which processes are responsible for colloid retention, primarily due to the paucity of visualization of pore scale unsaturated and transient flow experiments. Once these mechanisms are known, realistic sink terms can be formulated to describe colloid transport at the Darcy scale. Moreover, fundamental understanding of the interactions among colloids, grains, and solution chemistry will lead to more accurate and robust predictions of colloid transport under variable saturation, with implications for predicting and ultimately managing the mobility of contaminants and pathogens.

The objective of this study was to observe and clarify the mechanisms by which colloids are retained in partially saturated porous media. Using improved techniques and equipment with greater resolution, we were able to visualize individual colloidal particles and measure their velocities as well as to determine water film geometries, a significant improvement over our earlier work (*33*−*35*).

Experimental Section

Colloid retention was characterized at the pore scale using still and video visualization of the movement and retention of hydrophilic and slightly hydrophobic latex microspheres in quartz sand undergoing steady-state partially saturated flow. Two sets of visualization experiments were performed: Group A experiments determined the pore-scale distribution of water in the sand medium using bright field and confocal laser scanning microscopy, whereas Group B experiments used bright field microscopy to examine the pore-level flow patterns of colloids as well as visualization and quantification of colloid interception and retention.

Materials. The porous medium used for experiments was silica sand (0.85−1.70 mm, Unimin Corporation, NJ), that was acid cleaned (*51*), repeatedly rinsed in DDI water until the pH stabilized, and dried at 105 °C for 24 h. System pH levels were controlled by keeping the sand near pH 5.7. Colloidal synthetic microspheres (Magsphere, Inc., Pasadena, CA) examined are summarized in Table 1. Hydrophilic colloids were anionic carboxylated polystyrene microspheres (0.8, 2.6, or 4.8 μm diameters), colored red or blue as indicated. Colloids denoted as slightly hydrophobic were blue polystyrene 5.2 μm microspheres. Influent colloid solutions were prepared by diluting the stock colloid suspensions (10% initial concentration w/w) with DDI water; calculated influent colloid concentrations thus differed for each size particle: concentrations were 6.6×10^6 particles mL^{-1} for 4.8 μm colloids, 5.2×10^6 particles mL^{-1} for 5.2 μm colloids, and 2.6×10^6 particles mL^{-1} of each component in the mixed size tests. Colloid zeta (ζ) potentials were determined in DDI water (Laser Zee Meter model 501 m, PenKem, Bedford Hills, NY). Colloid contact angles were determined by measuring the interfacial angle of 10 μL DDI water droplets placed on horizontal cleaned glass slides coated with a dried layer of colloids. Droplets were imaged from the side using a CCD camera mounted on a bright field microscope reclined to a fully horizontal position.

Infiltration Chambers. Separate infiltration chambers (figures are shown in the Supporting Information) were needed for each visualization system due to the physical constraints of the viewing areas. The bright field system infiltration chamber was mounted at a 15° angle to enable unsaturated flow. To maintain partial saturation and to restrict any capillary fringe effects below the viewing area, a bottom vertical component of the chamber provided sufficient vertical displacement between the outlet and the 25-cm-long sloped observation area. To prevent finger flow from occurring, the sand chamber was limited to 2 cm width, and the sand layer thickness was 0.5 cm to allow sufficient light transmission.

Due to limited space under the confocal laser microscope, a second smaller chamber (1 cm × 4 cm inner sand chamber dimensions) was constructed. Porous ceramic plates (RH 1000-coarse pores, R&H Filter Co. Inc.) were mounted at the inlet and outlet of the chamber, and a syringe pump connected to the inlet was the influent source. Steady unsaturated flow was maintained using a peristaltic pump that provided constant suction at the effluent end.

TABLE 2. Experimental Parameters

expt	microscope	colloids used	water dye used
A1	confocal laser	none	0.1% fluorescein
A2	bright field	none	0.01% phenolsulfonphthalein red
B1	bright field	4.8 μm carboxylated blue hydrophilic	0.01% phenolsulfonphthalein red
B2		mixed carboxylated hydrophilic: combinations of 0.8 μm blue (some tests), 2.6 μm red, 4.8 μm blue	none
B3		5.2 μm polystyrene blue hydrophobic	none

Experiments and Procedures. Experiments in set A were carried out to determine the pore-scale distribution of water in sand. Experiment A1 (Table 2) was performed in triplicate using the confocal microscope. DDI water was added through the chamber's influent port until the sand was completely wetted. The chamber was placed under the confocal microscope, and the outlet pump was turned on to desaturate and maintain unsaturated conditions in the sand. The inlet syringe pump was then set to run at a flow rate of 0.15 mL min^{-1}. Once the system moisture content stabilized (as evidenced by meniscus stability), the influent was changed to 0.1% fluorescein solution (sodium salt) in DDI water. The water films surrounding grain surfaces were imaged at 5-μm *z*-axis increments.

The procedure used for filling and observing the bright field microscope infiltration chamber was the same for Experiments A2 and the B series, which examined the pore-level flow patterns of water as well as visualization and quantification of colloid retention. The chamber was set vertically, filled with clean dry sand to 18 cm height, and then laid flat for removal of the upper panel to facilitate imaging. The sand was completely wetted with the influent syringe pump, and the chamber was then allowed to drain for 30 min on the inclined mount. After initial drainage, steady-state unsaturated flow was established with a syringe pump at 0.15 mL min^{-1}, equivalent to a cross-sectional area-based rate of 1.5 mm min^{-1}. In Experiment A2 (carried out in triplicate) we investigated water flow through films using 0.01% phenolsulfonphthalein red dye in DDI. Images were taken at a point 10 cm from the top of the sand in the inclined chamber prior to and immediately following application of the red dye solution.

Colloid additions in experiments B1, B2, and B3 were superimposed on the steady state water flow by rapidly switching the water supply tube to a solution containing the colloids. Experiment B1 used hydrophilic 4.8-μm carboxylated blue colloids, whereas Experiment B2 used various combinations of 0.8-μm blue, 2.6-μm red, and 4.8-μm blue hydrophilic colloids. In Experiment B3, the relatively hydrophobic 5.2-μm blue colloids were applied. All experiments were conducted in triplicate.

In three experiments, the distribution of water content along the sand-filled channel was determined following colloid infiltration by sectioning the sand at 1-cm intervals and analyzing the moisture content gravimetrically, indicating saturated fractions of the total porosity (S) of 0.15−0.38 in the upper 10 cm and 0.46−0.64 at depths from 11 to 18 cm.

Imaging Systems. The visualization approach used by Crist et al. (*33*−*35*) was dramatically improved for this study by using an Olympus BX 50 transmitted light (bright field) microscope equipped with a high-resolution CCD camera. The microscope had 4× and 10× objective lenses (Olympus U Plan APO with numerical apertures (NA) of 0.16 and 0.4) that were able to fit in the space above the surface of packed sand. A 2× eyepiece was used, yielding an optical magnification of 20×, with subsequent digital zooming. Light from an integral illuminator (300-W halogen lamp) was aimed at a lens beneath the stage so that light was projected upward through the infiltration chamber. Maximum image resolution for the bright field system was 0.7 μm/pixel. MetaMorph Imaging System (version 6.1, Universal Imaging Corporation) software enabled image capture every 0.5 s, with images saved as still images (*.TIFF format) and/or arranged in sequences as stack files (*.STK format) that were subsequently converted to real-time "video" sequences.

Confocal microscopy optically sections a specimen, resulting in improved resolution and background discrimination, accomplished by using small confocal apertures to eliminate out-of-focus and background signals. The Leica TCS SP2 confocal microscope (HC PL APO 10.4× objective NA = 0.7, up to 4× zoom, maximum resolution of 0.5 μm/pixel) used for water film determinations in Experiment A1 was top-illuminated with a 488-nm argon laser for the exciting fluorescent-dyed water phase and a transmitted light channel to distinguish the sand grains. The maximum area examined (*xyz*) was 1.50 mm × 1.50 mm × 720 μm. Series of optical sections were obtained automatically with the integrated Leica Confocal Software (LCS) and either projected into a single image or reconstructed in 3-D.

Image Analysis. Water film characteristics and colloid retention were analyzed quantitatively using the integrated software packages mentioned above. For thresholding the images and counting the colloids, measurement routines coded for System KS400 (Zeiss Vision) were used. Images had to be segmented in order to detect the objects of interest and to obtain binary images for consecutive measurements. To accomplish the thresholding from the background, we took advantage of the fact that the colloids and the water phase were stained with blue, red, or fluorescent dye, depending on the microscope system used. Images obtained with the Olympus BX 50 microscope were 24-bit RGB format which could be segmented in the appropriate color channel (red or blue). Images obtained with the Leica confocal microscope were 8-bit gray images, with one image for every spectral channel. The water phase was detected using the fluorescent channel; the detection wavelength bandwidth could be adjusted in the operating software.

Segmentation was the most crucial step controlling the final result; staining the water phase and the colloids afforded the opportunity to minimize noise and measurement errors. The number and area of colloids were measured for each image in a measurement loop, which starts with the first image of a time series and measures the area and number of colloids. The process is then repeated sequentially for each image of the time series. One advantage of a measurement loop is that Boolean operations can be performed. For example, colloids which appear on two consecutive images at exactly the same position can be specified using the "AND" operator. Measuring the area is important because images obtained with a relatively low resolution may result in colloids appearing to clump together. Depending on the degree to which colloids covered the grain surfaces, the enumeration was based on a direct count or on the overall area of colloids divided by their size, which was known a priori.

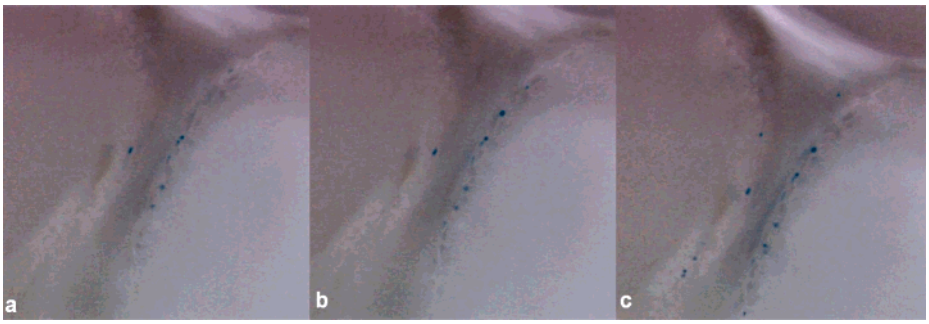

FIGURE 1. Evaporation effects on observed colloid deposition. Three sequential evaporation conditions imposed on a single imaging location: (a) low evaporation (humidified air, cover slip, illuminated only during image acquisition); (b) normal conditions; and (3) forced evaporation (heated air over imaged area).

TABLE 3. Video Clips Viewable in the Supporting Information (www.http://pubs.acs.org)

video	experiment number and title	related to figure
1	A1: 3D confocal reconstruction of water films and meniscii on sand grains	2
2	A2: dyed water movement along water films	3
3, 4	B1: Retention of hydrophilic colloids at AW_mS interface	5
5, 6	B2: Retention of mixed hydrophilic colloids at the AW_mS interface	6
7	B3: Retention of slightly hydrophobic colloids on grain surface (WS interface)	7e–f
8	B3: Retention of slightly hydrophobic colloids at the AW_mS and AW interfaces	7a–d
9	B3: Slightly hydrophobic colloids retained ingrain surface imperfections (WS interface)	-

Evaporation Effects. Objections about potential artifacts caused by evaporation from the exposed media surface have been raised (*52*). In previous testing (*53*) we have demonstrated that there appears to be little if any effect of such evaporation. First, as shown in the following section, observed retention phenomena are nearly instantaneous, often occurring within seconds of colloid-bearing liquid arrival in a given pore, far too rapid to be affected by normal evaporation conditions. Second, evaporation (typically on the order of mm day^{-1}) was judged to be a minor flux relative to the ongoing water flux of 0.15 mL min^{-1} through the already-moistened chamber. The video images cited below show a fluid and dynamic attachment/detachment environment, not one in which colloids are attaching as they are left stranded by quiescent receding water levels. More recently, specific testing was run with the bright field microscopy system (using 4.7-μm hydrophilic colloids) by imaging specific locations under three sequential potential evaporation conditions: (1) low evaporation—laminar flow of air humidified by passing it through a bubbler over the imaged area, a cover slip placed over the imaged area, and illumination turned on only during actual image acquisition; (2) normal conditions—using the normal operation practices described in the prior sections under constant illumination; and (3) forced evaporation—attempting to force evaporation effects with a heated air stream flowing over the imaged areas. To ensure treatment comparability, images were taken at fixed points in the chamber once colloid attachment reached equilibrium under the low evaporation regime, followed by the normal, and then forced evaporation regimes. The images in Figure 1, typical of those made during four replicate runs, showed no discernible difference in colloid attachment patterns between images taken under the low evaporation and normal operational regimes. (In contrast, the forced evaporation treatment, which was a radical departure from normal operating procedures, did result in observable increases in attachment, most apparent when quantification techniques were applied.) These tests were further evidence that the images and phenomena reported herein are valid.

Results and Discussion

Observations of water films on and between sand grains are presented first because colloid retention depends on the characteristics of the water films and resulting interfaces. The distribution of colloids within these water films is then discussed. While fully recognizing that there was variability among the individual pores observed, the figures shown were selected as representative based on extensive observation of both still and video images. Image quality varied for different experiments; those with good contrast and brightness that facilitate distinguishing the position of colloids on the interfaces are shown here. In addition to the still images presented in the figures, reference is made in Table 3 to video versions available via the Supporting Information link and at http://www.bee.cornell.edu/swlab/colloids/videos2/.

Experimental Set A: Water Film Configurations. As noted previously, film straining has been postulated as a colloid retention mechanism under partial saturation (*20*). To the best of our knowledge, measurements of film thicknesses on sand grains have not been carried out, leaving unresolved the question of whether films can retain colloids. Film thicknesses and meniscus shapes were determined from two-dimensional projections of a series of confocal microscope images acquired in Experiment A1. Figure 2 was selected as representative of images (from triplicate experiments, each imaging one location) that depict the configuration and thickness of the water films that exist on unsaturated sand grains. In plan view looking down on four sand grains denoted A, B, C, and D in Figure 2a, the grains are visible as black spheres covered with a green film of water. Between the grains are bright green water masses labeled 1, 2, and 3. Water masses 2 and 3 are pendular rings between grains B and C and B and D, respectively. Air-filled voids appear black. The laser confocal images can be visualized as cross-sections which allow determination of both the thickness of the water films covering the grains and the radii of the water menisci between the grains. Figure 2b is a cross section along vertical axis I in Figure 2a; Figure 2c is a cross section along horizontal axis II. (A three-dimensional reconstruction of Figure 2 can be viewed as Video 1 in the Supporting Information) The film thicknesses were not constant, ranging from less than 5 μm (atop grains high above the menisci) to approximately 25 μm on the areas of the grain surface near the meniscus attachment. The cross sections also clearly show that the surfaces of the grains are not smooth, otherwise the grain/water interface would have

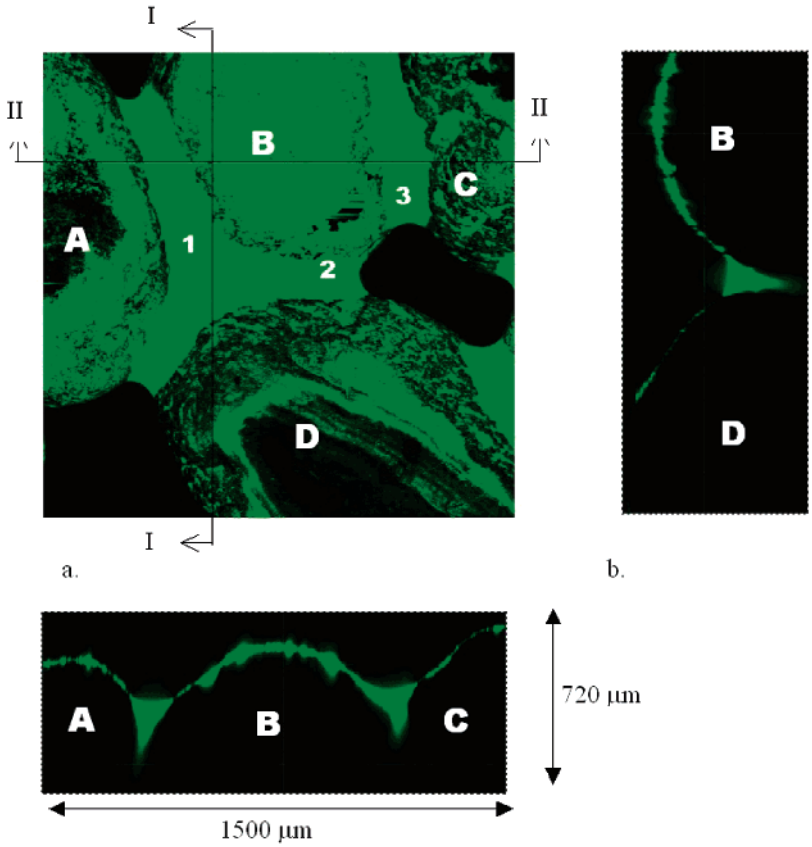

FIGURE 2. Position of water films in partially saturated sand; images taken with the confocal microscope along a fixed axis with a depth of 720 μm: (a) top view; (b) Section I; (c) Section II. Sand grains are labeled A, B, C, and D. Pendular rings are labeled 1, 2, and 3.

been smooth. The mean water meniscus radius was 108 ± 9 μm.

Although the precision of the film thickness determination was only 5 μm (the stepping increment of the confocal microscope), the films observed were many times greater than would be predicted from the matric potential in eq 1. The matric potential was not measured directly but can be calculated (eq 2) from the radius of the meniscus and the contact angle obtained from the confocal microscope images:

$$\Psi_m = \frac{2\sigma \cos \alpha}{r} \quad (2)$$

where Ψ_m is matric potential, α is contact angle, r is the radius (108 μm), and σ is the surface tension. For example, a radius of 108 μm and a contact angle of 35° yields a matric potential of −11 cm, and, via eq 1, a predicted film thickness of 20 nm, which agrees well with thicknesses estimated by Saiers and Lenhart (*30*). However, these theoretical film thicknesses are obviously orders of magnitude lower than the 5 to 25 μm thicknesses measured by confocal microscopy (Figure 2). The discrepancy likely arises from the theoretical assumption of equilibrium conditions in contrast to our case where the system, having recently been saturated, had not established equilibrium conditions. Thus it seems that the Hamaker equation (eq 1) cannot be used to calculate water film thickness under variable flow conditions, with the potential that colloids can indeed be immobilized in the thicker films we observed, as shown later.

The movement of water along water films was measured in Experiment A2 by introducing an instantaneous change from uncolored to red-dyed water at the same flow rate (no colloids present). The infiltration of the dye was observed with the bright field microscope; results typical of the 5 replicates run are shown in Figure 3 (as well as in Video 2 in the Supporting Information): Figure 3a (taken before the dye was introduced) shows three sand grains in contact with each other, with three pendular rings visible around the contact points of the grains, and an air bubble is located between the grains. Ten seconds after the application of dye at the inlet, grains A and B display a reddish tint (Figure 3b). At 20 s, meniscus 1 and grains A and B acquire a more distinct red color (Figure 3c). After 45 s the top of grain C near the pendular ring becomes tinted as well (Figure 3d). The red color around the grains clearly demonstrates that the water films covering the grains participate in the transport of water and dye. It is also important to note that the transport of dye over different grains was not uniform: whereas color arrived at grains A and B within 10 s, it required approximately 20 s for the dyed film on grain B to traverse 1 mm to begin coloring grain C. This suggests that the rapid arrival of dye at meniscus 1 on grains A and B occurred via a more rapid continuous water-filled pore path, rather than by film flow. In contrast, the slower arrival of dye at menisci 2 and 3 is attributed to connection with the dye source via film flow.

From these experiments we can estimate the relative contribution of film flow to the overall water flux. From Figure 3 we deduce that on the order of 30 s was required to renew the film of water in the pore. Assuming a film thickness of 10 μm and a grain diameter of 1 mm, the volume of water in the film around the grain is on the order of 0.03 mm^3 which, if renewed every 30 s, implies a flux on the order of 0.006 cm min^{-1}. Using the same calculation, a film thickness of 5 μm would imply a flux of 0.003 cm min^{-1}. This implies that, in view of the applied flux of 0.15 mm min^{-1} the water films carried only about 5% of the total flow. In contrast to the mechanism proposed (*20*) wherein film straining occurs only when pendular rings become disconnected at a critical level of saturation, these experiments suggest that there is a gradual change from pore flow to film flow.

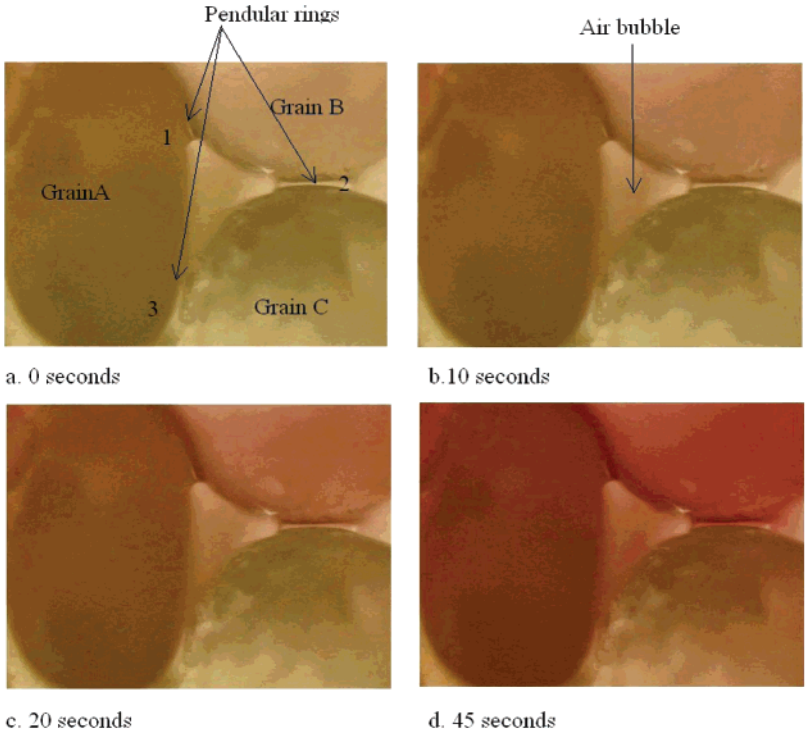

FIGURE 3. Determination of water film position and connections. Red dye was added to the steady state water flow (rate = 0.1 mL/min) at $t = 0$ s. Sand grains are labeled A, B, and C. Pendular rings are labeled 1, 2, and 3. These images were taken approximately 10 cm below the inlet port using the bright field microscope.

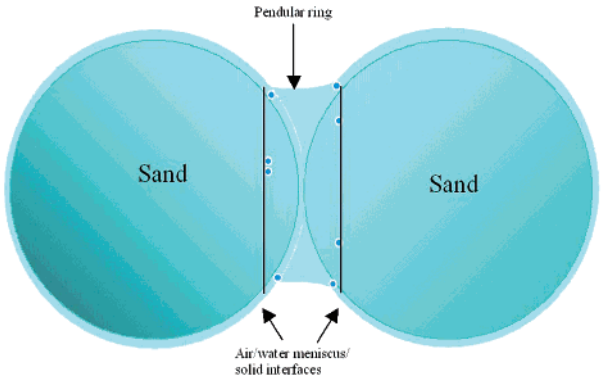

FIGURE 4. Conceptual diagram of air−water meniscus−solid (AW_mS) interfaces on two sand grains, and colloids retained at or near the AW_mS interfaces.

In previous work from our group, Crist et al. (*33*−*35*) reported colloid retention at the air−water−solid (AWS) interface based on visualizations with a system that had less magnification and lower resolution (2.2 μm/pixel). The experiments described here had far greater resolution (0.5 and 0.7 μm/pixel for the confocal and bright field systems, respectively) that allowed direct visualization of water films (Figures 2 and 3). From these experiments, it is evident that there is no true air/solid component of the interface because the grains are continuously covered with at least a thin film of water. There is thus no AWS interface where the water film ends. Therefore, the "AWS interface" concept is more correctly applied to the location on the grain surface where the water depth narrows to a film sufficiently thin to retain colloids, rather than an actual interface where the air, water, and solid are in joint contact. Thus, based on our visualizations, we propose the concept of the *air/water meniscus/solid interface*—here abbreviated AW_mS—shown conceptually in Figure 4, denoting the region where between-grain water menisci diminish to a thin water film on the grain surface. As shown below, it is at this AW_mS interface that colloid retention can occur.

Experimental Set B: Colloid Retention and Transport Mechanisms. *Experiment B1: 4.8-μm Hydrophilic Colloids.* These experiments with 4.8-μm hydrophilic colloids were run in triplicate, with each replicate imaged at seven locations. Observations of colloid behavior were consistent at all locations imaged, with attachment occurring almost solely at the AW_mS interfaces. For example, colloid retention is shown on two grains in Figure 5. The pendular ring between the grains curves downward below the focal plane on the right side of the images, making it difficult to clearly see the air−water interface. Over time, grain A (in the image focal plane) collected more colloids than grain B. By changing the focal plane, we determined that colloids were not being retained elsewhere on the surface of Grain A (Video 3). Several colloids attached to Grain B, but this was primarily in a region that was redder than the surrounding area, indicating the presence of more water. Accumulation of colloids at the AW_mS interface occurred rapidly, usually within one or two video frames (i.e., one second). For example, the particle indicated in Figure 6b (Video 4) slowed from 220 to 108 μm s^{-1} before suddenly stopping at the AW_mS. Although we could not quantify colloid distribution in the liquid phase, observations such as Videos 3 and 4 gave no indication that certain regions of flow carried more colloids than others.

Experiment B2: Mixed Hydrophilic Colloids. These experiments were run in duplicate, with each run being imaged at 6 locations. Typical deposition of blue 4.8-μm and red 2.6-μm hydrophilic colloids is shown in Figure 6a, where it can be seen that colloid attachment locations tended to vary with colloid size (i.e., color). It was estimated that 90% of overall colloid deposition occurred at the AW_mS interface where the water film is thicker, with 10% of deposition (consisting only of the smaller red colloids) in the thinner water film farther from the meniscus (Video 5). Additional runs that included only the largest and smallest (0.8-μm) colloids (Figure 6b and Video 6) indicated that the smaller

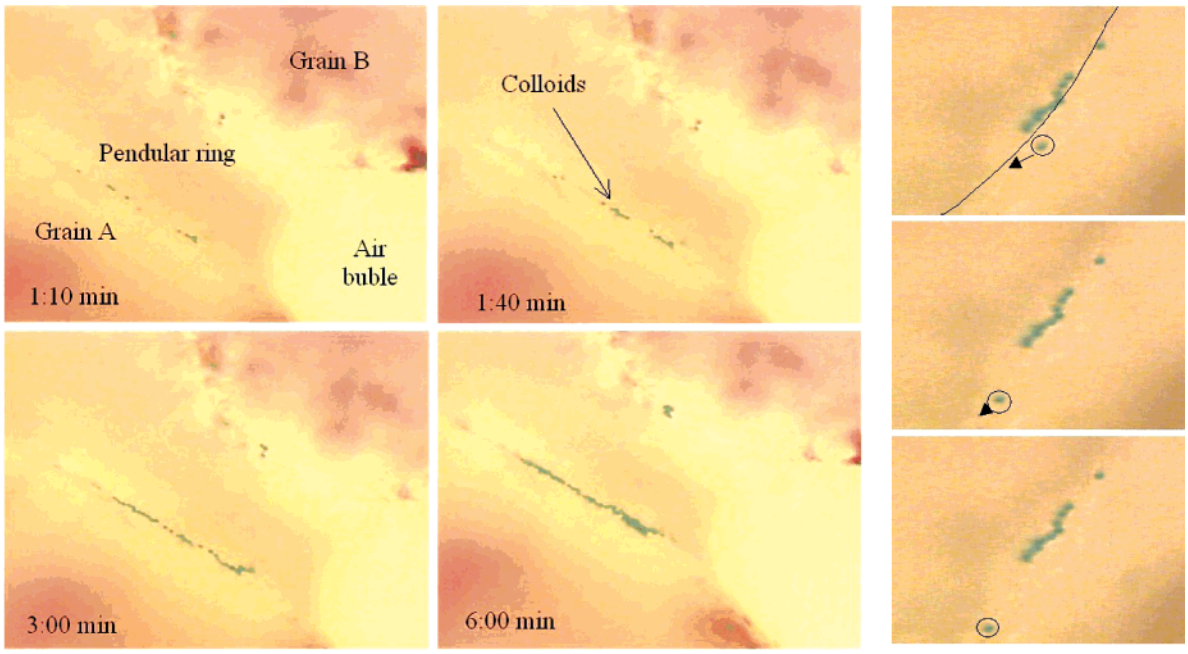

FIGURE 5. Hydrophilic colloid retention at AW_mS interfaces: (a) colloid accumulation (left); (b) colloid trajectory in the flow around an interface (black line); circles indicate a colloid as is slows and is immobilized in the final frame; time interval between frames = 0.5 s (right).

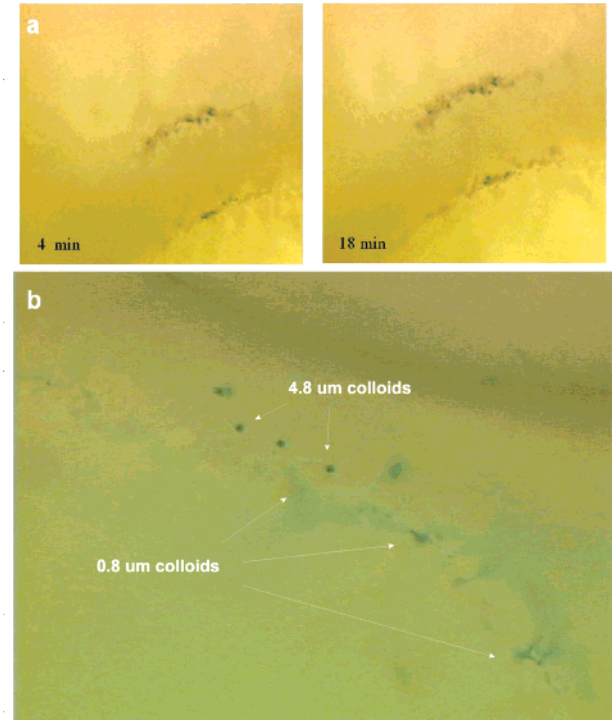

FIGURE 6. Mixed size hydrophilic colloid retention: (a) 4.8 μm (blue) and 2.6 μm (red) hydrophilic colloids, (b) blue 0.8 and 4.8 μm blue colloids, with the smaller colloids closer to the foreground and thus farther from the AW_mS interface.

colloids were distributed throughout the water film on the grain. These observations show that, as mentioned above, there was no true air/solid component of the AW_mS interface. The 0.8-μm colloids were small enough that, rather than all being trapped at the AW_mS interface, many could flow through the film along much of the grain surface. This confirms that the film thickness was the primary feature affecting colloid retention rather than an actual interface where the air, water, and solid are in contact, as previously assumed. In some cases, the water films were so thin that they could not transport the 0.8-μm colloids, particularly where menisci were attached to the side of the grain that was much lower than the top of the grain. This was consistent with Figure 3, where the thickness of the water film on the grain depended on the position of meniscus attachment. Thus, the potential for film straining depends on the relative position of meniscus attachment to the grain surface, making the phenomenon directly related to the moisture content and moisture potential.

Experiment B3: 5.2-μm Slightly Hydrophobic Colloids. Of 18 locations imaged (triplicate runs, each imaged at 6 locations) almost all observed retention occurred at AW_mS interfaces as shown in Figure 7. Two imaging locations showed apparent retention at AW interfaces, and three indicated some retention at the WS interface. In Figure 7a–d and video 8, colloids can be seen being retained close the AW_mS interface and at the AW interface. The observed retention at the AW interface was, in fact, colloids attaching other colloids already attached to the AW_mS interface, with the net effect of these additional colloids stringing out along the AW interface. However, the retention at the AW interface was not stable, as can be seen by comparing Figure 7c and d, which are more magnified images of the retention at Grain A; the instability of retention at this interface was even clearer in video time sequences. As noted, 3 of 18 locations imaged indicated some retention at WS interfaces, as shown in Figure 7e and f and Video 7, where three sand grains (labeled B, C, and D) are visible. The pattern of deposition varied with the flow regime within the pendular ring: colloids within the low velocity zone nearest the grain B surface moved slowly and were eventually deposited.

Preliminary Quantification of Colloid Retention. The results of Experimental Set B indicated two primary mechanisms for colloid retention: (1) retention at the AW_mS and, in some cases, WS interfaces; and (2) film straining of the smallest colloids. The focus of our preliminary quantification work was for the largest colloids at the AW_mS and WS interfaces, because, as noted above and consistent with our previous experiments (*34*, *35*), little stable retention occurred at the AW interface.

Colloids attaching at the AW_mS interface in Figure 5a were quantified, with results shown in Figure 8. Colloids were

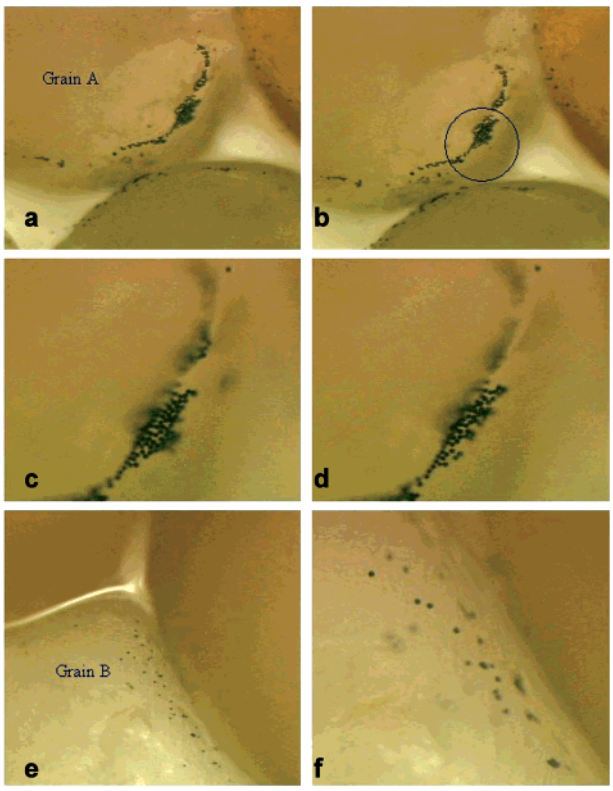

FIGURE 7. Retention of slightly hydrophobic colloids at AW_mS and AW interfaces (a−d) and on sand grain surfaces (e, f): (a) 12:00 min; (b) 13:00 min; (c) 13:30 min (detail of circled region in b); (d) 13:45 min; (e) sand grain surface, (f) detail of surface in image 7e.

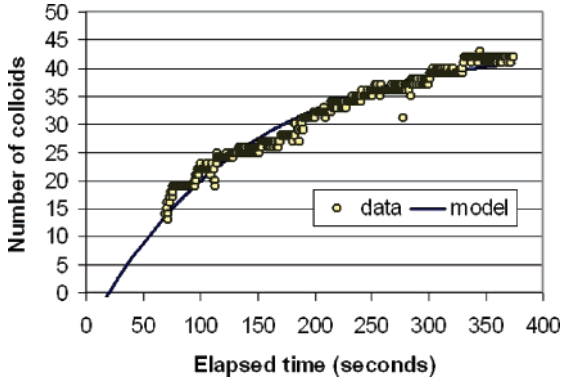

FIGURE 8. Colloid concentration at AW_mS interface (at 10 cm from the top of the sand column) as a function of time measured on real-time basis during infiltration, and colloid counts simulated with eq 3.

added at time $t = 0$, but early data were not available due to the time required for the microscope to target this particular location in the infiltration chamber. The variation in colloid accumulation in Figure 8 was caused by detachment/attachment processes: a given colloid that attached in one frame may detach in the next. Net colloid attachment generally increased until time $t = 250$ to 300 s. Beginning around 350 s, the net colloid attachment leveled off, meaning that the attachment and detachment rates were in equilibrium. The final image in Figure 6a coincides with the time that the AW_mS interface was "saturated", with new colloids able to attach only when a previously retained colloid detached. Colloid accumulation at the AW_mS interface can thus be described by a first-order reaction based on the available space for attachment at the interface:

$$M = M_o\,(1 - e^{-\beta(t-t^*)}) \qquad (3)$$

where M_o is the maximum number of colloids on the interface, t^* is the time at which the first colloid attaches (defined here as the distance from the inlet divided by the water velocity, equal to 20 s), and β is the first order rate constant attachment. This equation can be fitted to the data reasonably well with a resulting empirical β value of 0.0074 ($r^2 = 0.94$).

Colloid Retention Efficiencies. Although our experiments did not allow simultaneous measurements of colloid distributions in all focal planes of the liquid phase (which thus prevents estimation of collector efficiencies), visual observations in Experimental Set B suggested that the hydrophilic colloids appeared to be more evenly distributed across the mobile fluid phase (in accord with flow expected along streamlines) than the slightly hydrophobic colloids which tended to be concentrated near the AW and/or WS interfaces, consistent with recent observations (*54*). While we cannot definitively explain these initial observations and are currently conducting experiments to quantify them, it seems reasonable to speculate that the collector efficiency for the slightly hydrophobic colloids (flowing in close proximity to the interfaces and thereby increasing the possibility of collision) may be much greater than that for the more uniformly distributed hydrophilic colloids. This preliminary observation concurs with greater retention of hydrophobic colloids demonstrated in many breakthrough experiments (*19*−*23*, *30*, *43*, *55*).

Retention efficiencies at the AW and WS interfaces have been estimated by using DLVO (Derjaguin−Landau−Verwey−Overbeek) theory. Crist et al. (*35*) estimated the interfacial potential energies for hydrophilic and hydrophobic microspheres and suggested (as have others) that a substantial repulsive electrostatic energy barrier should prevent colloid attachment at the WS interface for both types of colloids. The absence of repulsive energy barriers for the interaction between hydrophobic colloids would favor rapid aggregation. However, it should be noted that the distances over which the attractive and repulsive forces occur are in the range of 20−100 nanometers, while the colloids were up to 5 μm in diameter (50−250 times as large). Figure 3 shows that imperfections on the grain surface are in the order of micrometers and should have therefore an influence as well, in accordance with findings of Ko and Elimelech (*56*) who postulated that the grain surface roughness influences the dynamics of particle deposition. Thus it seems that DLVO forces consisting of van der Waals and double layer potential energies under the low ionic strength conditions tested here have a lesser (but not negligible, as we shall see later) impact compared to other mechanisms in determining the retention efficiency. In the next section, we will derive what these additional forces are. In any case, the approach shown in eq 3 can be related to retention efficiency if the concentration of colloids in solution at the location of observation is known.

Interfacial Interactions. Interfacial interaction forces were estimated as the sum of the van der Waals, electric double layer, and hydrophobic interaction forces, as described in detail by Crist et al. (*35*), using a sphere−sphere model for colloid−colloid interactions (*57*) and a sphere−flat plate model for interactions of colloids with the air−water interface or the grain surface (*58*). The zeta potentials of all surfaces were negative for all colloids (Table 1). While calculations of interaction energies based on the properties of the colloids and media are useful to evaluate whether the patterns observed between experiments are in general agreement with an accepted theoretical framework, the limitations of quantitative interpretation of these models are well recognized, especially under repulsive conditions. The relative magnitude and direction of the interaction energy profiles we estimated for these experiments were similar to those presented in Crist et al. (*35*); however, because of the low ionic strength used

in the current experiments (colloids in distilled water), the total interaction energies extended over greater separation distances than in our previous study. Energy profiles for the hydrophilic colloids were repulsive except at very short separation distances (less than a nanometer). The magnitude of repulsion was much greater for the interaction of colloids (in water) with air or grains than for colloid−colloid interactions. This pattern is generally consistent with our observations that colloids did not attach to the AW interface. The lower energy barrier for colloid−colloid interactions is consistent with visual evidence of some limited interactions between colloids. For the slightly hydrophobic colloids, interaction with the AW interface was strongly repulsive at long distances, but became attractive at distances of a few nanometers. The energy barriers for interaction of the hydrophobic colloids with each other were much lower than for the colloid−AW interactions, but also became attractive at short separation distances. Thus, the estimates of the interfacial interaction energies are consistent with our visual observations that there is minimal interaction of colloids with the AW interface and grains (except for colloid retention in pits on grains, as we will see later), but that some colloid aggregation was evident.

The above discussion does not explain the observed retention at the AW_mS interface. To better understand forces retaining colloids at this interface, we combined the phenomena observed in Figures 2, 5, and 7. Referring to the configuration of colloids and water meniscus as drawn schematically in Figure 4, we assumed that kinetic energy associated with the velocity of moving colloids approaching the AW_mS interface can deform the meniscus by protruding it outward. This is based on the fact that the velocity of the colloids decreases rapidly as colloids approach and are retained at the AW_mS interface (Figure 5). Experiments with colloid movement in suspended films (*59*) showed that as long as the thickness of the film is less than the size of the particle, the water film surfaces are deformed and exert a force on the particle. This capillary (or immersion) force is directly related to the surface tension of the water and the extent of the deformation (*60*). The capillary forces resulting from the deformed film can be decomposed in a lateral force in the direction of flow and a force perpendicular to the grain surface for a colloid retained at the AW_mS interface. For colloids retained between two films (*59*), the non lateral forces cancel and a net force pushes the colloids back toward the bulk solution. Indeed, Sur and Pak (*59*) found that colloids in suspended films thinner than the colloid diameter were pushed toward deeper parts of the water film. However, for colloids at the AW_mS interface, the force perpendicular to the grain surface will result in friction forces that will resist movement back to the bulk solution. Thus it is likely that, in our experiments, the colloids were immobilized against the grain surface by friction, which in turn suggests that grain roughness would affect retention at the AW_mS interface. The fact that both hydrophilic and slightly hydrophobic colloids were retained at the AW_mS interface would be expected, since, according to the theory presented by Kralchevsky and Nagayama (*57*), although the degree of hydrophobicity affects the shape of the deformed surface, in all cases there will be a net lateral force into the bulk solution and a net force perpendicular to the grain surface. The slightly hydrophobic colloids immobilized at the AW_mS interface served as attachment points for additional colloids encountering them in the flowing water. The attachment between these colloids reflects the absence of repulsive interaction energy barriers between hydrophobic colloids (*35*). However, the attached colloids were easily sheared off by physical forces when the string of colloids became too long and reached a location where the velocity in the water was greater. Capillary forces may also play a role since this process only occurs near the AW_mS interface. Kralchevsky and Nagayama (*57*) and Sur and Pak (*59*) found that when two particles approach each other (by chance) even at a distance of 100 μm, the deformation surfaces around the two particles merge into a single larger deformation surface.

The attachment mechanism at the WS interface cannot be explained by the DLVO theory (under the low ionic strengths tested here) but becomes apparent when we consider the imperfections on the grain as we saw in the water film experiments (Figure 2). To see if these irregularities were a realistic mechanism for retention, we found several sequences (of which Video 9 was the clearest; still version shown as Figure SI-3 in the Supporting Information) which shows that colloids were retained in small depressions or pits in the grain surface. The process of attachment differs from that observed at the AW_mS interface. In the video sequence a colloid was observed moving slowly along the surface of the grain as part of low velocity laminar flow. After it traveled for some time, it deflected sideways and it appeared to roll into a depression on the grain, in contrast to the attachment behavior observed at the AW_mS interface where the colloids were suddenly slowed due to resistance of the film.

Future Work. These experiments have provided valuable insights into colloid behavior in unsaturated sand, having identified the importance and potential mechanism of colloid retention at the AW_mS interfaces where water menisci thicknesses are similar to colloid diameters. In addition, we identified some retention in grain surface imperfections at the WS interface. The study also provides an initial insight into why retention of hydrophobic colloids is usually greater than that of hydrophilic colloids in unsaturated soils. Many questions remain to be resolved in future experiments, including determination of the influences of surfactants, grain water repellency, and grain surface roughness.

Acknowledgments

Partial funding for this work was provided by the Cornell Biocomplexity and Biogeochemistry Initiative.

Supporting Information Available

Figures of bright field imaging system, confocal laser infiltration chamber, and retention of colloids at grain surface imperfections; video clips from various experiments. This material is available free of charge via the Internet at http://pubs.acs.org.

Literature Cited

(1) Ryan, J. N.; Elimelech, M. Colloid mobilization and transport in groundwater. *Colloids Surf. A* **1996**, *107*, 1−56.
(2) Zachara, J. M.; Flury, M.; Harsh, J. Colloid-facilitated migration of radioelements—Mechanisms, significance, and needed conditions. *Geochim. Cosmochim. Acta* **2002**, *66* (15A), A867
(3) McCarthy, J. F.; McKay, L. D.; Bruner, D. D. Influence of ionic strength and cation charge on transport of colloidal particles in fractured shale saprolite. *Environ. Sci. Technol.* **2002**, *36* (17), 3735−3743.
(4) Grolimund, D.; Barmettler, K. Colloid-facilitated transport of pollutants: Phenomena and modeling. *Geochim. Cosmochim. Acta* **2002**, *66* (15A), A293.
(5) Flury, M.; Mathison, J. B.; Harsh, J. B. In situ mobilization of colloids and transport of cesium in Hanford sediments. *Environ. Sci. Technol.* **2002** *36*, 5335−5341.
(6) Zhuang, J.; Flury, M.; Jin, Y. Colloid-facilitated Cs transport through water-saturated Hanford sediment and Ottawa sand. *Environ. Sci. Technol.* **2003**, *37* (21), 4905−4911.
(7) Loveland, J. P.; Bhattacharjee, S.; Ryan, J. N.; Elimelech, M. Colloid transport in a geochemically heterogeneous porous medium: aquifer tank experiment and modeling. *J. Contam. Hydrol.* **2003**, *65* (3−4), 161−182.
(8) Elimelech, M.; Chen, J. Y.; Kuznar, Z. A. Particle deposition onto solid surfaces with micropatterned charge heterogeneity: The "hydrodynamic bump" effect. *Langmuir* **2003**, *19* (17), 6594−6597.
(9) Weisbrod, N.; Niemet, M. R.; Selker, J. S. Light transmission technique for the evaluation of colloidal transport and dynamics in porous media. *Environ. Sci. Technol.* **2003**, *37* (16), 3694−3700.

(10) Zhuang, J.; Flury, M.; Jin, Y. Comparison of Hanford Colloids and Kaolinite Transport in Porous Media. *Vadose Zone J.* **2004**, *3* (2), 395−402.
(11) Vilks, P.; Frost, L. H.; Bachinski, D. B. Field-Scale Colloid Migration Experiments in a Granite Fracture. *J. Contam. Hydrol.* **1997**, *26* (1−4), 203−214.
(12) McCarthy, J. F.; Zachara, J. M. Subsurface Transport of contaminants. *Environ. Sci. Technol.* **1989**, *23* (5), 496−502.
(13) Kersting, A. B.; Efurd, D. W.; Finnegan, D. L.; Rokop, J. J.; Smith, D. K.; Thompson, J. L. Migration of plutonium in groundwater at the Nevada Test Site. *Nature* **1999**, *397* (6714), 56−59.
(14) Toran, L.; Palumbo, A. V. Colloid transport through fractured and unfractured laboratory sand columns. *J. Contam. Hydrol.* **1992**, *9* (3), 289−903.
(15) Noell, A. L.; Thompson, J. L.; Corapcioglu, M. Y.; Triay, I. R. The role of silica colloids on facilitated cesium transport through glass bead columns and modeling. *J. Contam. Hydrol.* **1998**, *31*, 23−56.
(16) Harter, T.; Wagner, S.; Atwill, E. R. Colloid transport and filtration of *Cryptosporidium parvum* in sandy soil and aquifer sediments. *Environ. Sci. Technol.* **2000**, *34*, 62−70.
(17) Elimelech, M.; Nagai, M.; Ko, C.-H.; Ryan, J. N. Relative insignificance of mineral grain zeta potential to colloid transport in geochemically heterogeneous porous media. *Environ. Sci. Technol* **2000**, *34* (11), 2143−2148.
(18) Wan, J.; Wilson, J. L. Visualization of the role of the gas−water interface on the fate and transport of colloids in porous media. *Water Resour. Res.* **1994**, *30* (1), 11−23.
(19) Wan, J.; Wilson, J. L. Colloid transport in unsaturated porous media. *Water Resour. Res.* **1994**, *30* (4), 857−864.
(20) Wan, J.; Tokunaga, T. K. Film straining of colloids in unsaturated porous media: conceptual model and experimental testing. *Environ. Sci. Technol.* **1997**, *31* (8), 2413−2420.
(21) Wan, J.; Tokunaga, T. K. Measuring partition coefficients of colloids at air−water interfaces. *Environ. Sci. Technol.* **1998**, *32*, 3293−3298.
(22) Schafer, A.; Ustohal, P.; Harms, H.; Stauffer, F.; Dracos, T.; Zehnder, A. J. B. Transport of bacteria in unsaturated porous media. *J. Contam. Hydrol* **1998**, *33*, 149−169.
(23) Thompson, S. S.; Flury, M.; Yates, M. V.; Jury, W. A. Role of the air−water−solid interface in bacteriophage sorption experiments. *Appl. Environ. Microbiol.* **1998**, 304−309.
(24) Thompson, S. S.; Yates, M. V. Bacteriophage inactivation at the air−water−solid interface in dynamic batch systems. *Appl. Environ. Microbiol.* **1999**, 1186−1190.
(25) Jewett, D. G., Logan, B. E.; Arnold, R. G.; Bales, R. C. Transport of *Pseudomonas* fluorescents strain P17 through quartz sand columns as a function of water content. *J. Contam. Hydrol.* **1999**, *36*, 73−89.
(26) Jin, Y.; Chu, Y. J.; Li, Y. S. Virus removal and transport in saturated and unsaturated sand columns. *J. Contam. Hydrol.* **2000**, *43*, 111−128.
(27) Gamerdinger, A. P.; Kaplan, D. I. Physical and chemical determinants of colloid transport and deposition in water-unsaturated sand and Yucca mountain tuff material. *Environ. Sci. Technol.* **2001**, *35*, 2497−2504.
(28) Saiers, J. E.; Lenhart, J. J. Ionic-strength effects on colloid transport and interfacial reactions in partially saturated porous media. *Water Resour. Res.* **2003**, *39* (9), 1256−1269.
(29) Saiers, J. E.; Lenhart, J. J. Colloid mobilization and transport within unsaturated porous media under transient-flow conditions. *Water Resour. Res.* **2003**, *39* (1), 1−12.
(30) Wan, J.; Tokunaga, T. K. Partitioning of clay colloids at air−water interfaces. *J. Colloid Interface Sci.* **2002**, *247*, 54−61.
(31) Sirivithayapakorn, S. S.; Keller, A. Transport of colloids in unsaturated porous media: A pore-scale observation of processes during the dissolution of air−water interface. *Water Resour. Res.* **2003**, *39* (12), 1346, 1−10.
(32) Crist, J. T.; Zevi, Y.; Taylor, J.; Peranginangin, N.; Gao, B.; Lyon, S.; Dittrich, T. M., Marshall, A. G.; DeAlwis, D.; Baveye, P. C.; Parlange, J.-Y.; McCarthy, J. F.; Steehuis, T. S. Visualization of colloidal transport in porous media. *DIAS Report Plant Production no 80, Colloids and Colloid-Facilitated Transport of Contaminants in Soils and Sediments, Tjele, Denmark*. 2002; pp 31−38.
(33) Crist, J. T.; McCarthy, J. F.; Zevi, Y.; Baveye, P. C.; Throop, J. A.; Steenhuis. T. S. Pore-scale visualization of colloid transport and retention in partly saturated porous media. *Vadose Zone J.* **2004**, *3* (2), 444−450.
(34) Crist, J. T.; Zevi, Y.; McCarthy, J. F.; Troop, J.; Steenhuis, T. S. Transport and retention mechanisms of colloids in partially saturated porous media. *Vadose Zone J.* **2005**, *4*, 184−195.
(35) van der Lee, J.; Ledoux, E.; de Marsily, D. Modeling of colloidal uranium transport in a fractured medium. *J. Hydrol.* **1992**, *139*, 135−158.
(36) Corapcioglu, M. Y.; Jiang, S. Colloid-facilitated groundwater contaminant transport. *Water Resour. Res.* **1993**, *29*, 2215−2226.
(37) Song, L.; Elimelech, M. Transient deposition of colloidal particles in heterogeneous porous media. *J. Colloid Interface Sci.* **1994**, *167* (2), 301−313.
(38) Swanton, S. W. Modelling colloid transport in groundwater; the prediction of colloid stability and retention behaviour. *Adv. Colloid Interface Sci.* **1995**, *54*, 129−208.
(39) Grindrod, P.; Lee, A. J. Colloid migration in symmetrical nonuniform fractures: article tracking in three dimensions. *J. Contam. Hydrol.* **1977**, *27* (3−4), 157−175.
(40) Sun, N.; Walz, J. Y. A model for calculating electrostatic interactions between colloidal particles of arbitrary surface topology. *J. Colloid Interface Sci.* **2001**, *234* (1), 90−105.
(41) Corapcioglu M. Y.; Choi, H. Modeling colloid transport in unsaturated porous media and validation with laboratory column data. *Water Resour. Res.* **1996**, *32* (12), 3437−3449.
(42) Lenhart, J. J.; Saiers, J. E. Transport of silica colloids through unsaturated porous media: experimental results and model comparisons. *Environ. Sci. Technol.* **2002**, *36* (4), 769−777.
(43) Saiers, J. E. Laboratory observations and mathematical modeling of colloid-facilitated contaminant transport in chemically heterogeneous systems. *Water Resour. Res.* **2002**, *38* (4) 3-1−3-14.
(44) Darnault, C. J. G.; Steenhuis, T. S.; Garnier, P.; Kim, Y.-J.; Jenkins, M. B.; Ghiorse, W. C.; Baveye, P. C.; Parlange, J.-Y. *Vadose Zone J.* **2004**, *3*, 262−270.
(45) Yao, K.-M.; Habibian, M. T.; O'Melia, C. R. Water and wastewater filtration: concepts and applications. *Environ. Sci. Technol.* **1971**, *5* (11), 1105−1112.
(46) Elimelech, M.; O'Melia, C. R. Kinetics of deposition of colloidal particles in porous media. *Environ. Sci. Technol.* **1990**, *24* (10), 1528−1536.
(47) Chu, Y.; Jin, Y.; Flury, M.; Yates, M. V. Mechanisms of virus removal during transport in unsaturated porous media. *Water Resour. Res.* **2001**, *37* (2), 253−263.
(48) Veerapaneni, S.; Wan, J.; Tokunaga, T. K. Motion of particles in film flow. *Environ. Sci. Technol.* **2000**, *34*(12), 2465−2471.
(49) Iwamatsu, M.; Horii, J. Capillary condensation and adhesion of two wetter surfaces. *J. Colloid Interface Sci.* **1996**, *182*, 400−406.
(50) Litton, G. M.; Olson, T. M. Colloid deposition rates on silica bed media and artifacts related to collector surface preparation methods. *Environ. Sci. Technol.* **1993**, *25*, 185−193.
(51) Wan, J.; Tokunaga, T. K. Comment on "Pore-Scale Visualization of Colloid Transport and Retention in Partly Saturated Porous Media". *Vadose Zone J.* **2005** (in press).
(52) Steenhuis, T. S.; McCarthy, J. F.; Crist, J. T.; Zevi, Y.; Baveye, P. C.; Throop, J. A.; Fehrman, R. L.; Dathe, A.; Richards, B. K. Reply to the Comments of J. Wan and T. K. Tokunaga on "Pore-Scale Visualization of Colloid Transport and Retention in Partly Saturated Porous Media". *Vadose Zone J.* **2005** (in press).
(53) Jin, Y.; Lazouskaya, V. Micromodel study of colloid interfacial retention with application to colloid transport in unsaturated porous media. *Geophys. Res. Abstr.* **2005**, 7 (09565).
(54) Wan, J.; Tokunaga, T. K Surface-zone flow along unsaturated rock fractures. *Water Resour. Rese.* **2001**, *37* (2), 287−296.
(55) Ko, C. H.; Elimelech, M. The shadow effect in colloid transport and deposition dynamics in granular porous media: Measurements and mechanisms. *Environ. Sci. Technol* **2000**, *34*, 3681−3689.
(56) Hogg, R.; Cahn, D. S.; Healy, T. W.; Fuerstenau, D. W. Diffusional mixing in ideal system. *Chem. Eng. Sci.* **1966**, *21*, 1025−1038.
(57) Norde W.; Lyklema, J. Protein adsorption and bacterial adhesion to solid-surfaces − a colloid-chemical approach. *Colloids Surf.* **1989**, *38*, 1−13.
(58) Sur, J.; Pak, H. K. Capillary force on colloidal particles in a freely suspended liquid thin film. *Phys. Rev. Lett.* **2001**, *86* (19).
(59) Kralchevsky, P. A.; Nagayama, K. Capillary interaction between particles bound to interfaces. Liquid films and biomembranes. *Adv. Colloid Interface Sci.* **2000**, *85*, 145−192.

Received for review September 9, 2004. Revised manuscript received June 23, 2005. Accepted June 28, 2005.

ES048595B